Water Research 216 (2022) 118351

Contents lists available at ScienceDirect

Water Research

journal homepage: www.elsevier.com/locate/watres

Eggshell membrane derived nitrogen rich porous carbon for selective electrosorption of nitrate from water

Jiao Chen [a,b,#], Kuichang Zuo [b,c,d,#,*], Yilin Li [e], Xiaochuan Huang [b,d], Jiahui Hu [a], Ying Yang [b], Weipeng Wang [b,f], Long Chen [f], Amit Jain [b,e], Rafael Verduzco [b,e], Xiaoyan Li [a], Qilin Li [b,c,d,e,f,*]

[a] Shenzhen Engineering Research Laboratory for Sludge and Food Waste Treatment and Resource Recovery, Tsinghua Shenzhen International Graduate School, Tsinghua University, China

[b] Civil and Environmental Engineering, Rice University, MS 319, 6100 Main Street, Houston, Texas 77005, USA

[c] The Key Laboratory of Water and Sediment Sciences, Ministry of Education; College of Environment Sciences and Engineering, Peking University, Beijing 100871, China

[d] NSF Nanosystems Engineering Research Center Nanotechnology-Enabled Water Treatment, Rice University, MS 6398, 6100 Main Street, Houston, Texas 77005, USA

[e] Department of Chemical and Biomolecular Engineering, Rice University, MS 362, 6100 Main Street, Houston, Texas 77005, USA

[f] Department of Materials Science and Nano Engineering, Rice University, 6100 Main Street, Houston, Texas 77005, USA

ARTICLE INFO

Keywords:
Eggshell membrane
Nitrate selectivity
Electrosorption
Nitrogen functional groups
Density functional theory

ABSTRACT

Nitrate (NO_3^-) is a ubiquitous contaminant in water and wastewater. Conventional treatment processes such as adsorption and membrane separation suffer from low selectivity for NO_3^- removal, causing high energy consumption and adsorbents usage. In this study, we demonstrate selective removal of NO_3^- in an electrosorption process by a thin, porous carbonized eggshell membrane (CESM) derived from eggshell bio-waste. The CESM possesses an interconnected hierarchical pore structure with pore size ranging from a few nanometers to tens of micrometers. When utilized as the anode in an electrosorption process, the CESM exhibited strong selectivity for NO_3^- over Cl^-, SO_4^{2-}, and $H_2PO_4^-$. Adsorption of NO_3^- by the CESM reached 2.4×10^{-3} mmol/m^2, almost two orders of magnitude higher than that by activated carbon (AC). More importantly, the CESM achieved NO_3^-/Cl^- selectivity of 7.79 at an applied voltage of 1.2 V, the highest NO_3^-/Cl^- selectivity reported to date. The high selectivity led to a five-fold reduction in energy consumption for NO_3^- removal compared to electrosorption using conventional AC electrodes. Density function theory calculation suggests that the high NO_3^- selectivity of CESM is attributed to its rich nitrogen-containing functional groups, which possess higher binding energy with NO_3^- compared to Cl^-, SO_4^{2-}, and $H_2PO_4^-$. These results suggest that nitrogen-rich biomaterials are good precursors for NO_3^- selective electrodes; similar chemistry can also be used in other materials to achieve NO_3^- selectivity.

1. Introduction

Nitrate (NO_3^-) contamination in drinking water sources is a growing concern worldwide (Almasri, 2007). Despite its relatively low acute toxicity, NO_3^- is a precursor for nitrite and nitrosamine that are carcinogenic and can cause stomach cancer (Kälble et al., 1990). Excessive uptake of nitrate >30 ppm can inhibit growth, impair the immune system, and cause stress in aquatic species (Romano and Zeng, 2007). In addition, as a nutrient, excess concentration of NO_3^- in water can cause eutrophication and algal blooms, resulting in anoxia and dead zones that can be highly detrimental to ecosystem health. The maximum concentration of NO_3^- in drinking water recommended by the World Health Organization (WHO) is 50 mg/L; the U.S. Environmental Protection Agency (EPA) sets the maximum permissible NO_3^- concentration at 45 mg/L (or 10 mg/L as N) in drinking water (Pastushok et al., 2019). Major sources of nitrate pollution include wide-spread use of nitrogen fertilizers for agriculture, discharge of municipal and industrial wastewaters, processed food, dairy and meat products, and leakage of livestock and poultry excreta (Gan et al., 2019; Kim and Choi, 2012; Uzun and Debik, 2019). Several technologies have been used to remove NO_3^- from water, including biological denitrification, ion exchange, reverse osmosis (RO), and electrodialysis (Ruiz-Beviá and Fernández-Torres, 2019). These approaches have shown success in specific application scenarios, but they each have limitations. For example, biological

* Corresponding authors.
E-mail addresses: kuichang.zuo@pku.edu.cn (K. Zuo), qilin.li@rice.edu (Q. Li).
# These authors contributed equally to this work.

https://doi.org/10.1016/j.watres.2022.118351
Received 25 November 2021; Received in revised form 9 March 2022; Accepted 21 March 2022
Available online 22 March 2022

treatment is slow and requires large reactors and complex operation. It is difficult to scale down to small systems. Ion exchange requires high concentrations of harsh chemicals such as alkaline for regeneration, the subsequent disposal of which has major environmental impact (Li et al., 2015; Meng et al., 2014). RO and electrodialysis can achieve high NO_3^- removal, but they also remove almost all other common ions (e.g., Na^+, Cl^-, Ca^{2+}, SO_4^{2-}), which are often present at concentrations orders of magnitude higher than NO_3^-, leading to significant overtreatment and hence high energy consumption.

Electrosorption processes such as capacitive deionization (CDI) are simple and chemical-free. They have attracted interest for their capability of removing ionic contaminants as well as desalinating brackish water (Chen et al., 2015; Suss et al., 2015). In electrosorption, ions adsorb on the oppositely charged electrode during adsorption period and desorb when a zero or reversed voltage is applied, producing desalinated water and brine in alternating cycles (Zuo et al., 2018). Although conventional carbon electrodes remove charged species non-selectively through electrostatic interaction, selective removal of target contaminants including Ca^{2+}, SO_4^{2-}, and heavy metals, and high value metals has been demonstrated using functionalized carbon, selective ion-exchange membranes and coatings (D.I. Kim et al., 2019; Zuo et al., 2018), and novel materials such as metal organic frameworks (Zuo et al., 2020). Several recent studies have demonstrated selective electrosorption of NO_3^- . For example, a carbon electrode coated with anion exchange resins containing amine functional groups realized a selectivity of 3.39 for NO_3^- over Cl^- and 2.3 times higher NO_3^- adsorption than the uncoated carbon electrode (Kim and Choi, 2012). Activated carbon electrode functionalized with quaternary amine surfactant (cetyltrimethylammonium bromide) achieved a NO_3^- to Cl^- selectivity of 7.7 in an passive inverted CDI cell without an applied electric field (Oyarzun et al., 2018). In addition, because NO_3^- is more weakly solvated compared with Cl^- and SO_4^{2-}, slit micropores have been created in activated carbon to match the planar structure of dehydrated NO_3^- to achieve selective electrosorption of NO_3^- through the ion sieving effect (Hawks et al., 2019). These studies suggest that amine-functionalization and pore manipulation are effective approaches to improve NO_3^- selectivity in electrosorption.

Eggshell membrane (ESM) is a natural biomass source available from food industry waste. As a porous membrane with unique three-dimensional microstructures, ESM has been used as an adsorbent to remove heavy metals from water, including hexavalent chromium, mercury, silver, and cadmium (Liu and Huang, 2011; Sha Wang, 2013; Sunho Park, 2016). ESM can also be easily carbonized, and the carbonized eggshell membranes (CESM) can be used as electrode materials for electrochemical energy storage and conversion due to its high porosity as well as high electric conductivity (Geng et al., 2015; Li et al., 2014, 2012; Rath et al., 2014). In addition, the protein network in ESM results in high nitrogen content in CESM, which has been reported to improve electrochemical properties such as conductivity (Deng et al., 2016; Ismagilov et al., 2009; Ji et al., 2018), specific capacitance and wettability (Li et al., 2018; Shen and Fan, 2013; Xu et al., 2017, 2019; Yang et al., 2019)

In this study, we for the first time apply the CESM in an electrosorption process for removal of NO_3^- from water that contains common competing anions such as Cl^-, SO_4^{2-} and $H_2PO_4^-$. The electrosorption behavior of CESM for various anions was comprehensively evaluated in single- and multi- solute solutions to evaluate its selectivity. The NO_3^-/Cl^- selectivity achieved was compared with those reported in previous publications, and the mechanism of selectivity was elucidated using density function theory (DFT) calculation.

2. Materials and methods

2.1. Materials and chemicals

Powdered activated carbon (AC) CEP21K was purchased from Power Carbon Technology Co., Ltd., Republic of Korea. The cation exchange membrane (CEM) was purchased from ASTOM, Japan. The graphite sheet used as the current collector was purchased from Mineral Seal Corporation, USA. NaCl (>99.0%), $NaNO_3$ (>99.5%) and Na_2SO_4 (>99.0%) were purchased from EMD Millipore Corporation; $NaH_2PO_4{\cdot}H_2O$ (99.8%) was purchased from the Fisher Scientific; Hydrochloric acid (HCl, 37%), polyvinyl alcohol (PVA, molecular weight 89,000−98,000 g/mol), and glutaraldehyde (GA, 25 wt% solution in water) were purchased from Sigma-Aldrich. Fresh eggs were purchased from a local supermarket (H.E.B in Houston). Deionized water (resistivity > 18 MΩ) was used to prepare all aqueous solutions.

2.2. Electrode fabrication and characterization

After removing the albumen and yolk of the eggs, the eggshell was immersed in 0.1 M HCl solution overnight to obtain ESM by etching away inorganic components (mainly $CaCO_3$) (Fig. 1a). The eggshell membrane was then rinsed with DI water and dried in an oven at 60 °C overnight. The ESM was cut into 5 cm × 1 cm coupons and pyrolyzed in a tubular furnace under argon atmosphere with a gas flow rate of 80 mL/min. The temperature was increased from room temperature to 200 °C, then 600 °C at a rate of 1 °C/min and 4 °C/min, respectively, and was held at 600 °C for another 2 h, after which the furnace was turned off and cooled to room temperature. The resulting CESM samples were utilized as electrodes in an electrosorption cell for further tests.

The AC electrode was prepared following our previously reported method (Jain et al., 2018; D.I. Kim et al., 2019; Zuo et al., 2020). It contained 90 wt% of AC and 10 wt% of GA-crosslinked PVA polymeric binder. To prepare the AC electrode, GA was firstly mixed with PVA (6 wt%) at 4.4 mol% relative to PVA repeating unit. Then AC powder and DI water were added slowly into the PVA-GA solution to prepare a slurry with a final solid content of about 30 wt%. After mixing overnight, the slurry was cast onto a graphite sheet using a custom-made flow coater, with a blade gap of 300 μm and a coating rate of 1 mm/s. The electrode was dried in air and cross-linked in a vacuum oven at 80 °C for 2 h before use.

The CESM and AC electrodes were characterized by high-resolution field emission scanning electron microscopy (SEM, Quanta FEG 250, Thermo Fisher Scientific, USA) for surface morphology. Brunauer–Emmett–Teller (BET) surface area (m^2/g) and total pore volume (cm^3/g) were determined by N_2 adsorption and desorption (Quantachrome Autosorb-Iq-MP/Kr, USA). The surface chemistry was analyzed by Fourier transform infrared spectroscopy (FTIR, Nicolet iS50, Thermo Scientific, USA). The elemental information was obtained using X-ray photoelectron spectroscopy (XPS, PHI Quantera, Japan) coupled with a PHI Quantera SXM scanning X-ray microprobe. A two-electrode chronopotentiometry was performed on a potentiostat system (CHI660E, CHI instruments, USA) to evaluate the specific electric capacitance (C, F/g) of CESM and AC. During the test, two pieces of CESM (total mass of 40 mg) or AC (total mass of 50 mg), each of 5 cm × 1 cm in size, were dipped in an electrolyte solution containing 2 mM NaCl or 2 mM $NaNO_3$. The applied cathodic/anodic current was 10^{-5} A, and the high/low voltage was 1/0 V. The specific capacitance was calculated using Eq. 1 (Wang et al., 2017):

$$C = \frac{I\Delta t}{m_e \Delta U} \tag{1}$$

Here, I is the applied constant current (10^{-5} A), Δt is the average time (s) of the charge period, m_e is the mass of CESM or AC (g), and ΔU is the voltage range (1 V) during the charge/discharge process.

2.3. Electrosorption experiments

The electrosorption cell consists of a rectangular acrylic housing, a pair of titanium current collectors, a rubber gasket and a plastic mesh that form the flow channel, a CESM working electrode, and an AC

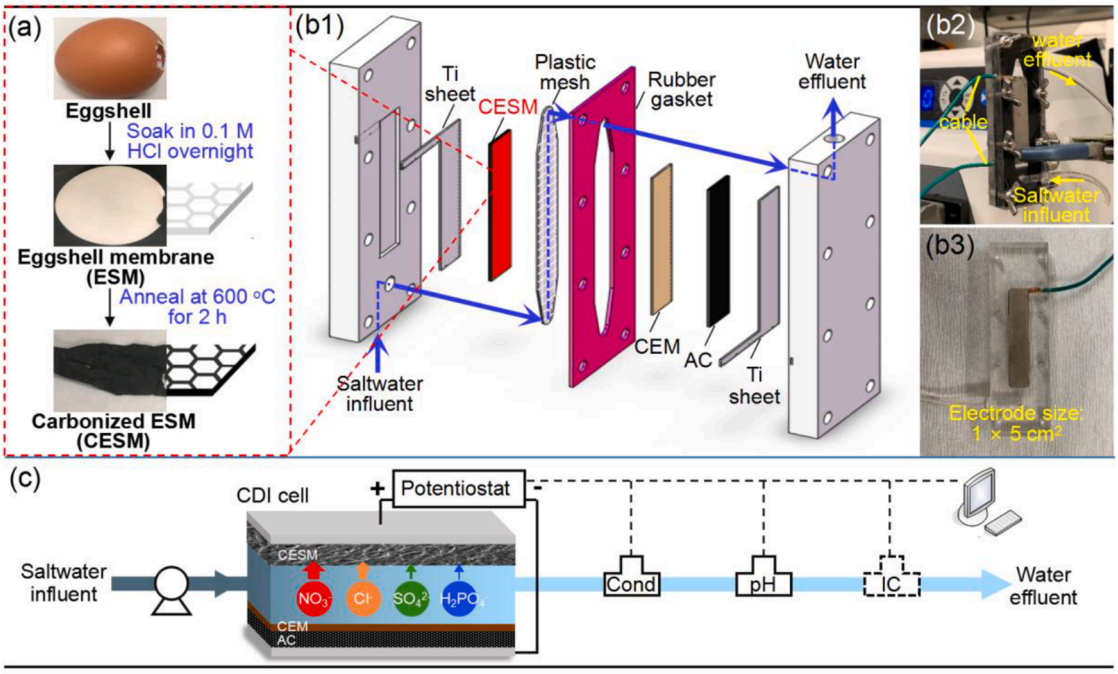

Fig. 1. Preparation of CESM and its operation in an electrosorption cell. (a) Preparation of CESM from eggshell; (b) Schematic (b1) and photographs (b2–3) of the electrosorption cell; (c) Schematic of the experimental system. CEM: cation exchange membrane; AC: activated carbon; Cond: inline conductivity meter; pH: inline pH meter; IC: effluent anion concentrations are determined by ion chromatography.

counter electrode (Fig. 1b). Because an AC electrode was used as the control anode and was tested using another AC electrode as the cathode, the CESM anode was also tested using the same AC cathode. Both the AC and CESM electrodes have a dimension of 1 cm × 5 cm, and a CEM was installed between the AC electrode and the mesh separator to enhance charge efficiency. Considering an anion exchange membrane (AEM) may have different permeability for various anions, no AEM was utilized so that the actual selectivity of AC and CESM materials could be evaluated.

During operation, a CESM (70.0 ± 0.3 mg) or AC (55.8 ± 0.1 mg including PVA binder but excluding the graphite sheet) electrode was used as the anode, and an AC electrode was used as the cathode. The electrosorption cell was operated in continuous flow mode (Fig. 1c), with single solute (2.0 mM) or multi-solute (0.5 mM for each of the 4 solutes) feed solutions containing $NaNO_3$, NaCl, Na_2SO_4 and/or $NaH_2PO_4{\cdot}H_2O$ flowing between two electrodes at a flow rate of 1.0 mL/min for all experiments. The pH of the multi-solute solution is 5.6, the temperature is 26 °C. A constant voltage of 1.2 V or −1.2 V was applied to the electrodes using a potentiostat (CHI660E, CH instruments, USA), and the adsorption and desorption period were both set at 30 min corresponding to a water recovery of 50%. The current, effluent conductivity, and effluent pH were continuously monitored and recorded using the potentiostat, a micro conductivity meter (ET908, eDAQ, Australia), and a pH meter (PC2700, OAKTON, USA), respectively, at a time interval of 1 s. Effluent water samples were taken every 3 min and analyzed for anion concentrations using ion chromatography (IC, ICS2000, DIONEX, USA).

Ion removal performance of the electrodes was assessed first by individual anion removal (*AR*, mmol/g, Eq. (2)) during an adsorption cycle. Charge efficiency (*CE*) quantifies the percentage of the applied charges utilized for salt removal during the adsorption cycle, and was calculated using Eq. (3) (Zuo et al., 2018). The energy consumption for nitrate removal was calculated using Eq. 4.

$$AR = \frac{Q\int_0^T \left(C_{i,inf} - C_{i,eff}\right)dt}{m_e} \tag{2}$$

$$CE = \frac{FQ\int_0^T \left[\left(C_{Cl^-,inf} - C_{Cl^-,eff}\right) + \left(C_{NO_3^-,inf} - C_{NO_3^-,eff}\right) + 2\left(C_{SO_4^{2-},inf} - C_{SO_4^{2-},eff}\right) + \left(C_{H_2PO_4^-,inf} - C_{H_2PO_4^-,eff}\right)\right]dt}{\int_0^T Idt} \tag{3}$$

$$EC = \frac{I{\cdot}U{\cdot}T}{AR_{NO_3^-}{\cdot}m_e} \tag{4}$$

Here, Q (L/s) is the flow rate of the feed water; $C_{i,\ inf}$ (M) and $C_{i,\ eff}$ (M) represent the influent and effluent concentration of ion i respectively; T is the duration of each adsorption circle (1800s); t (s) is operation time; F (96,485 C/mol) is Faraday's constant; I (A) is the electric current; m_e (g) and A_e (m^2) are the mass or surface area of the AC or CESM electrode. U (V) is the voltage during the adsorption period; $AR_{NO3\text{-}}$ (mmol/g) is the nitrate removal during an adsorption cycle.

Selectivity ($S_{i/j}$) between two competing ions i and j is defined by Eq. (5), where the numerator and denominator represent the ratio between the solid phase concentration (or amount adsorbed) and the influent concentration (i.e., equilibrium aqueous phase concentration at adsorption saturation) of ions i and j, respectively.

$$S_{i/j} = \frac{\int_0^T (C_{i,inf} - C_{i,eff})dt \Big/ C_{i,inf}}{\int_0^T (C_{j,inf} - C_{j,eff})dt \Big/ C_{j,inf}} \quad (5)$$

2.4. DFT calculations

Density function theory calculation was performed for graphene structures containing four types of nitrogen functional groups including pyridine, pyrrol, oxidized pyridine, and quaternary nitrogen species. These molecular systems were optimized in terms of geometry and frequency. Calculations were performed in Gaussian 16 using B3LYP/6–311+G^{**} to obtain the binding energy and molecular distance between the nitrogen in the carbon matrix and the different anions. The damping scheme of Becke and Johnson (Grimme, 2011; Johnson and Becke, 2005), simplified as DFT-D3 (BJ) was adapted to correct for intermolecular interactions. The solvation effect of water was described by a density based solvation model (Marenich et al., 2009). An external electric field of 2.4 kV/m (4.67×10^{-9} a.u.) was added along the direction of adsorption. Atom partial charge and electrostatic potential were simulated using Mulliken electronic population analysis (Mulliken, 1955) and visual molecular dynamics (Humphrey et al., 1996), respectively. The binding energy was defined as the difference in total energy between the reactants (nitrogen species and the anions) and the product (nitrogen/anion complex). The molecular distance was defined as the closest distance between the nitrogen species and the various anions.

3. Results and discussion

3.1. Physicochemical characteristics of the CESM

The eggshell membrane is a ~25 μm thick Janus membrane consisting of a highly porous network of proteins on the inner side, and a thin dense layer (~1 μm) of proteins on the outer side facing the inorganic eggshell (Fig. 2a1&S1). After carbonization, the porous structure of the inner layer was well preserved (Fig. 2a2-a3), while the dense outer layer became porous and interconnected with the inner layer network (Fig. 2a4-a5). Detailed SEM characterization showed that the porous CESM network consisted of interconnected fibers with a diameter of 1–3 μm, forming pores with size ranging from 0.5 to 4 μm. N_2 adsorption/desorption isotherm showed that the cumulative pore volume of CESM was 0.0284 cm^3/g, and the pores were mostly mesopores with three distinct pore size ranges centered at 2.6, 4.3 and 7.7 nm, respectively (Fig. 2b). The hierarchical pore structure with pore sizes ranging from several micrometers (macropores) to a few nanometers (mesopores) provide channels for effective ion migration (Han et al., 2019; Lytle et al., 2011). The high interconnectivity of the network was also conducive to efficient electron transfer (Li et al., 2012). Nevertheless, as the CESM was not activated, its specific surface area was only 13.0 m^2/g. This was comparable with previous report for a CESM carbonized at 700 °C (17.0 m^2/g) (Li et al., 2012), but much lower than AC (2103.7 m^2/g, Fig. 2b).

The FTIR spectrum of the AC powder was smooth with few peaks, indicating a high degree of carbonization (Fig. 2c). As a comparison, the spectrum of ESM showed the presence of abundant oxygen- (-OH at 3200–3500 cm^{-1}, C = O at 1637 cm^{-1}, and C—O at 1078 cm^{-1}) (Arami et al., 2006; Kong and Yu, 2007; Tsai et al., 2006; Zhang et al., 2015) and nitrogen- containing functional groups, as indicated by the C—N stretching/N—H bending (1528 cm^{-1} for amide II and 1230 cm^{-1} for amide III), and C = $N_{(Ar)}$ (1313 cm^{-1}) peaks (Liang et al., 2014; Liu and Huang, 2011). After carbonization at 600 °C, most oxygen functional groups were removed by dehydration, decarboxylation, and decarbonylation reactions, while most nitrogen functional groups were preserved in the CESM (Fig. 2c). XPS analyses further confirmed that the high N content (13.3 wt%) and the N/C atomic ratio (14%) in the CESM (Fig. 5a) in contrast to the activated carbon (< 0.2% N).

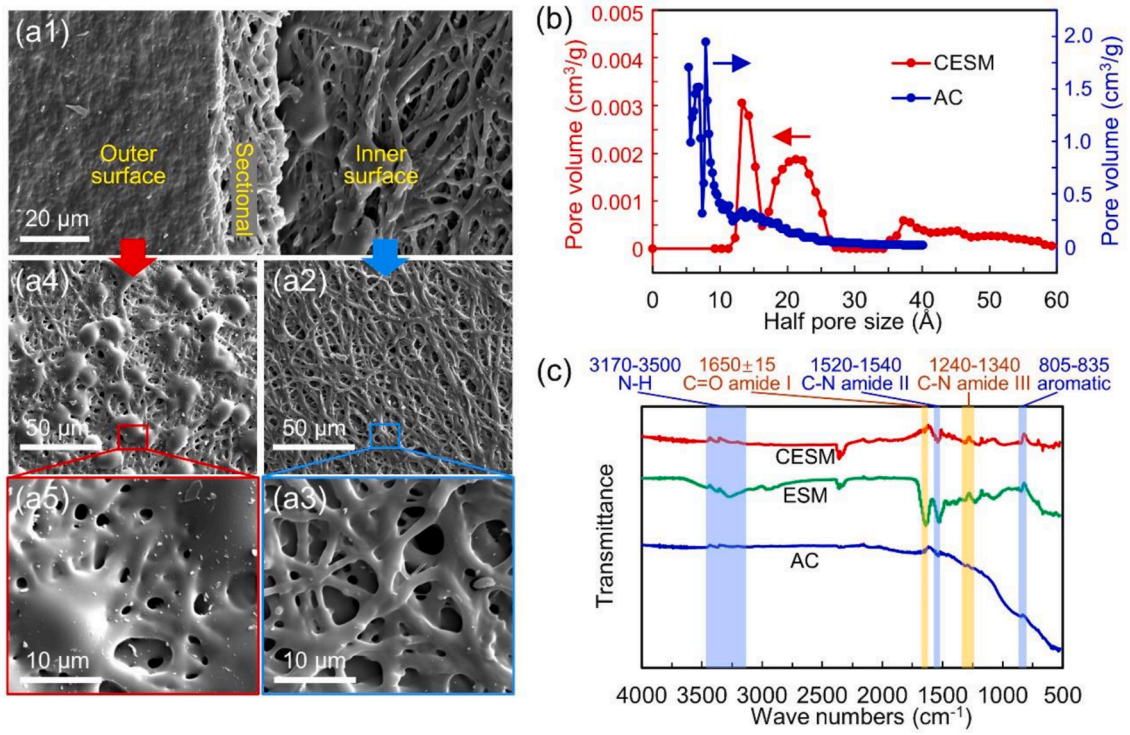

Fig. 2. Characteristics of CESM and AC. (a1) SEM image of an ESM overlapped on another ESMs, with the left and middle part showing the outer surface and sectional area of an ESM, respectively, and the right part showing the inner surface of another ESM; (a2–3) SEM images of the CESM inner surface; (a4–5) SEM images of the CESM outer surface; (b) Pore size distribution of CESM and AC powder; (c) FTIR spectra of AC, ESM and, CESM.

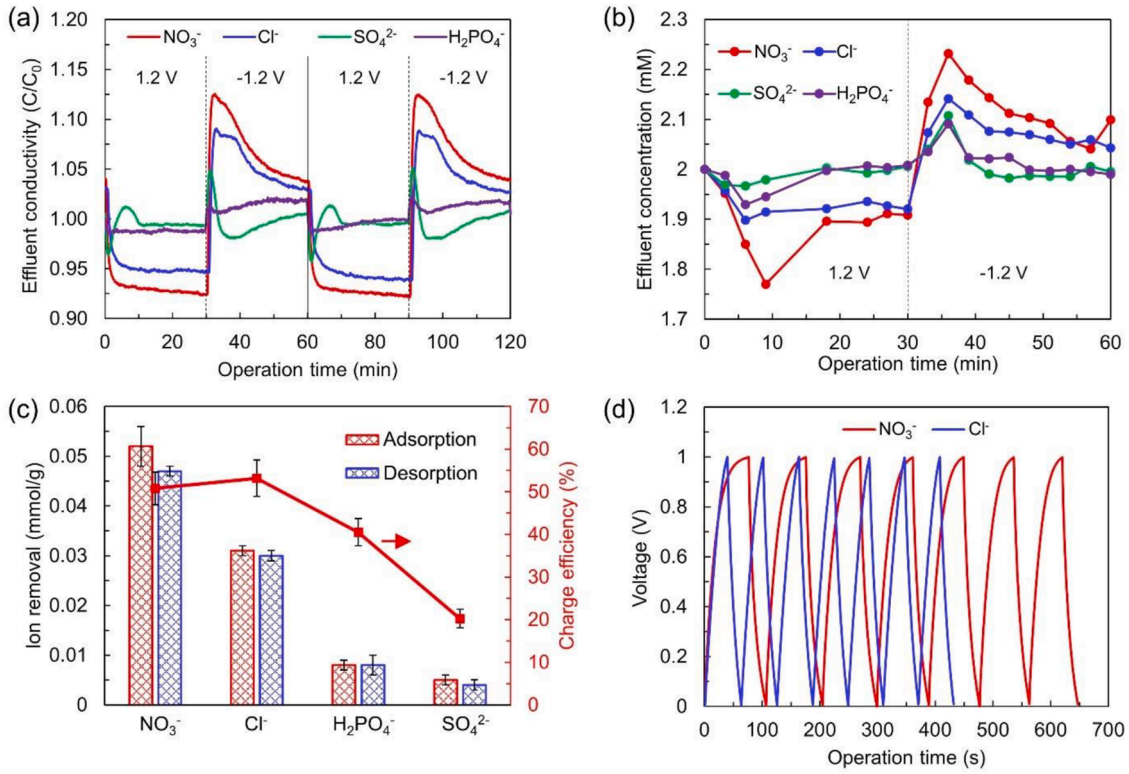

Fig. 3. Electrosorption performance of the CESM electrode in single solute solutions. (a) Effluent conductivity and (b) effluent anion concentration during adsorption and desorption periods; (c) Anion adsorption/desorption amount and charge efficiency of the CESM electrode in different single solute solutions; (d) Chronopotentiometry profiles of the CESM electrode in NaCl and $NaNO_3$ solutions (electrolyte concentration = 2.0 mM; current = 10^{-5} A).

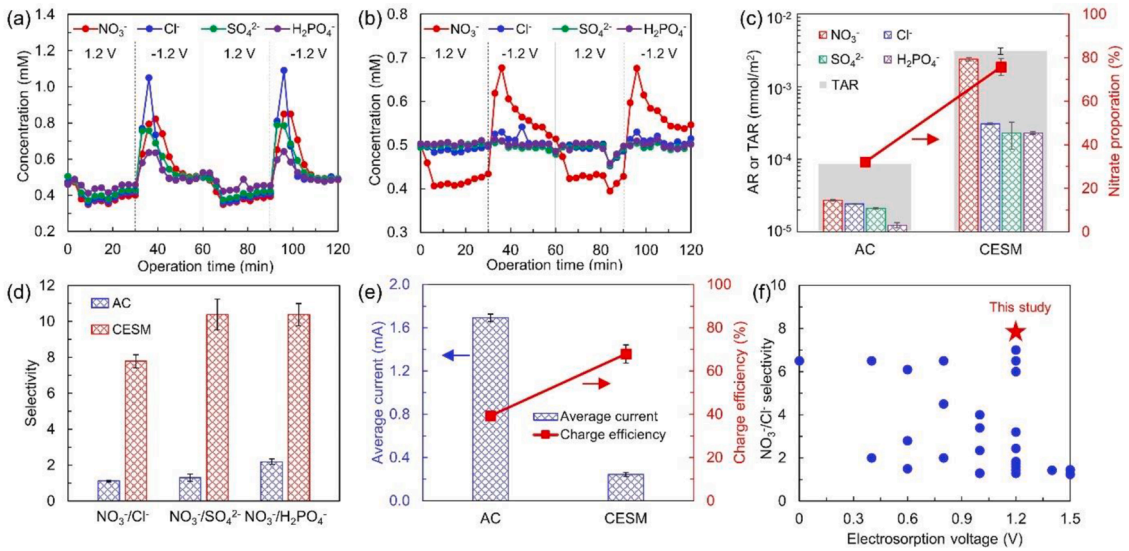

Fig. 4. Performance of the AC and CESM electrodes in electrosorption of multi-solute solutions. Effluent ion concentrations of (a) AC and (b) CESM electrode during adsorption and desorption cycles; (c) Anion removal (AR, mmol/m^2), total anion removal (TAR, mmol/m^2), and nitrate removal proportion in the AC and CESM electrosorption systems; (d) Selectivity for NO_3^- over Cl^- (NO_3^-/Cl^-), SO_4^{2-} (NO_3^-/SO_4^{2-}), and $H_2PO_4^-$ ($NO_3^-/H_2PO_4^-$) on AC and CESM electrodes; (e) Average current and charge efficiency in the AC and CESM electrosorption systems; (f) Literature review on NO_3^-/Cl^- selectivity at various applied electrosorption voltage. Data used in the figure can be found in Table 1.

3.2. *Electrosorption for single solute solutions*

The electrosorption performance of the CESM and AC electrodes were evaluated using single solute solutions containing 2.0 mM NaCl, $NaNO_3$, Na_2SO_4, or $NaH_2PO_4{\cdot}H_2O$. As shown in Figs. 3a and S2, reproducible current, effluent conductivity, and pH profiles were obtained for the CESM electrode during the adsorption and desorption cycles. A "frequency doubling" effect (Ahualli et al., 2019; Porada et al., 2013) occurred for SO_4^{2-}, because SO_4^{2-} possessed twice the charge of the other anions and caused fast release of co-ions (Na^+) during the adsorption period. As the system was operated in a continuous flow mode, effluent conductivity decreased during the adsorption period and

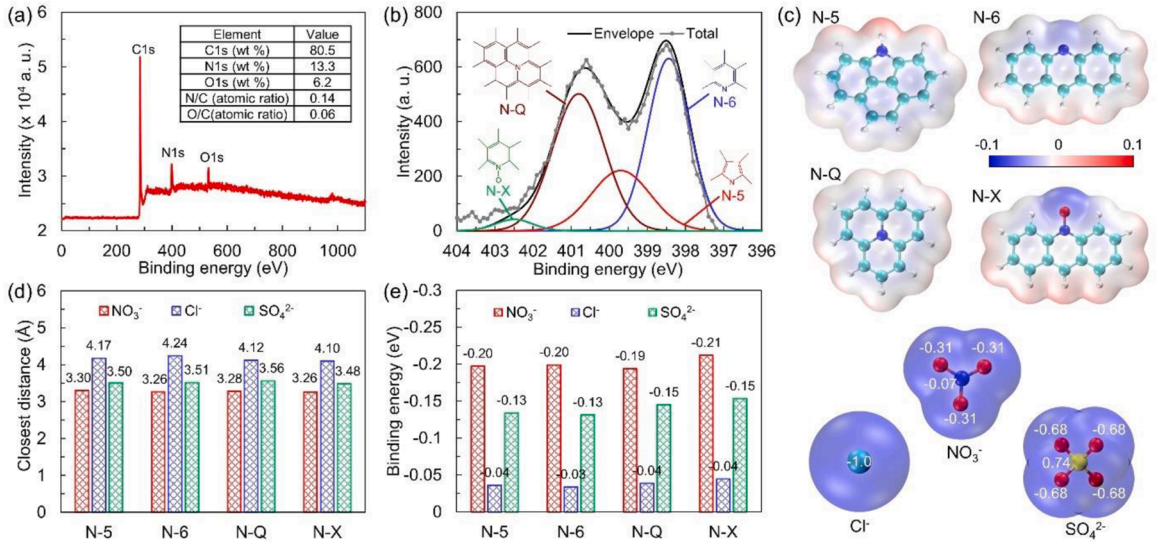

Fig. 5. Mechanism analysis for nitrate selective removal on CESM. (a) Full XPS spectra of CESM; (b) N1s spectra of CESM with four types of nitrogen species split; (c) Molecular structure and charge distribution of the four N species and various anions; (d) The closest distance between nitrogen species and each anion; (e) DFT calculation of binding energy between N species and each anion.

increased during the desorption period at −1.2 V (Fig. 3a), despite that the initial conductivities were different for different solutions. The changes in conductivity for $NaNO_3$ and NaCl solutions were much higher than that for Na_2SO_4 or NaH_2PO_4 solution, and the conductivity change in the $NaNO_3$ solution was even greater than that in the NaCl solution, indicating higher adsorption of NO_3^- than the three other anions. Effluent anion concentrations determined by IC exhibited a trend consistent with the conductivity profiles (Fig. 3b), with single solute adsorption following the order of NO_3^- (0.052 ± 0.004 mmol/g) > Cl^- (0.031 ± 0.001 mmol/g) > $H_2PO_4^-$ (0.008 ± 0.001 mmol/g) > SO_4^{2-} (0.005 ± 0.001 mmol/g) (Fig. 3c). Because $H_2PO_4^-$was the dominant phosphate species at pH 4.5–5.5, $H_2PO_4^-$ concentration was used to represent total phosphate . Furthermore, adsorption of all ions was highly reversible, with almost complete release of the adsorbed ions during the desorption cycle (Fig. 3b&c). It was noted that, although the hydrated radius of Cl^- is smaller than NO_3^- and the equivalent concentration of SO_4^{2-} was twice that of NO_3^-, the adsorption of NO_3^- on CESM was much higher than that of Cl^- and SO_4^{2-}, suggesting that the CESM had different affinity towards the various anions. The electric capacitance of the electrode was further characterized by chronopotentiometry. As shown in Fig. 3d, the CESM electrode exhibited a much higher electric capacitance in $NaNO_3$ solution (4.3 ± 0.2 mF/g) than in NaCl solution (3.0 ± 0.3 mF/g), consistent with the greater electrosorption of NO_3^- by the CESM electrode. According to Eq. 1, the higher capacitance in $NaNO_3$ than in NaCl shows that the CESM has higher adsorption capacity of NO_3^- than Cl^-, suggesting that the CESM has more electrosorption sites for NO_3^- than Cl^-, which will be further discussed in the following sections. The single solute adsorption by the AC electrode also exhibited highly reproducible adsorption and desorption behavior during the charging and discharging periods (Fig. S3). However, anion adsorption on the AC anode followed the order of Cl^- (0.133 ± 0.003 mmol/g) > NO_3^- (0.107 ± 0.002 mmol/g) > SO_4^{2-} (0.071 ± 0.003 mmol/g) > $H_2PO_4^-$ (0.016 ± 0.003 mmol/g) (Figure S3), different from the CESM that had the highest electrosorption for NO_3^-. Chronopotentiometry experiments further confirmed that the AC electrode had a much higher electric capacitance in the NaCl solution (7.8 ± 0.6 mF/g) than in the $NaNO_3$ solution (2.8 ± 0.2 mF/g) (Fig. S4). It should be noted that the specific surface area of CESM (13.0 m^2/g) was less than 1% of that of AC (2103.7 m^2/g), yet its electric capacitance was 154 and 38% that of AC in $NaNO_3$ and NaCl, respectively. The electrode mass normalized adsorption of NO_3^- on the CESM (0.052 ± 0.004 mmol/g) was 48.6% of that on the AC (0.107 ± 0.002 mmol/g), but the surface area normalized NO_3^- adsorption (4.0×10^{-3} mmol/m^{-2}) was 78.4 times that of the AC (5.1×10^{-5} mmol/m^{-2}). These results suggest an extremely high adsorption capacity and electric capacitance per unit surface area of the CESM, especially when NO_3^- was utilized as charge carrier.

Comparable current was produced during the adsorption and desorption periods for all four solutions (Fig. S2&S5). Since the CESM has higher ion adsorption for NO_3^- and Cl^- (Fig. 2c), it also produced higher current in NO_3^- and Cl^- solutions (Fig. S5). Charge efficiencies for CESM were 50.8, 53.2, 40.5, and 20.2% in the NO_3^-, Cl^-, $H_2PO_4^-$ and SO_4^{2-} solution, respectively (Fig. 3c). These charge efficiencies were relatively low compared to conventional membrane CDI (>90%). Nevertheless, the charge efficiency of CESM in NO_3^- and Cl^-solutions were clearly higher than that in SO_4^{2-} and $H_2PO_4^-$ solutions, due to the lower cation (i.e., Na^+) concentration (Suss et al., 2015). The low charge efficiencies were caused by the absence of an anion exchange membrane on the CESM surface, which allowed adsorption and release of co-ions (i.e., Na^+) on the anode during the desorption and adsorption cycles, respectively. In addition, as SO_4^{2-} and phosphate species possess more charges than Cl^- and NO_3^-, they would cause more and faster release of co-ions during the adsorption period, resulting in lower charge efficiency than in NO_3^- and Cl^- containing solutions. This phenomenon was also observed in our previous study, where charge efficiency was lower in a $CaCl_2$ solution than in a NaCl solution of the same molar concentration (Kim et al., 2019). In addition, the hydrated size and hydration energy of NO_3^- (0.335 nm in radius, −300 kJ/mol) and Cl^- (0.332 nm, −340 kJ/mol) are also smaller compared to SO_4^{2-} (0.379 nm, −1080 kJ/mol) and $H_2PO_4^-$ (0.450 nm, −465 kJ/mol) (Hawks et al., 2019; Marcus, 1991), which leads to higher mobility and better access to adsorption sites.

3.3. Electrosorption of multi-solute solutions

In natural water or wastewater, background anions such as Cl^- and SO_4^{2-} would compete with NO_3^- for adsorption sites on the electrode. To evaluate the impact of common competing anions, electrosorption experiments were carried out using a multi-solute solution containing 0.5 mM each of $NaNO_3$, NaCl, Na_2SO_4, and $NaH_2PO_4{\cdot}H_2O$. As shown in Fig. S6 & 4a-b, reproducible effluent conductivity, pH, and effluent ion concentrations were observed during repeated adsorption and

desorption cycles using either the CESM or the AC electrode as the anode. The conductivity change was much higher when using AC than CESM anodes, indicating higher amount of ion adsorption/desorption due to larger surface area of the AC electrode material. Measurement of anion concentrations showed that the removal of NO_3^-, Cl^-, SO_4^{2-} and $H_2PO_4^-$ by the AC electrode was 0.057 ± 0.001, 0.051 ± 0.001, 0.044 ± 0.001 and 0.026 ± 0.002 mmol/g, respectively, during the adsorption period, while the total anion removal (TAR) reached 0.178 mmol/g (Fig. S7). In contrast, the removal of NO_3^-, Cl^-, SO_4^{2-} and $H_2PO_4^-$ by the CESM was 0.031 ± 0.002, 0.004 ± 0.001, 0.003 ± 0.001, 0.003 ± 0.001 mmol/g, respectively, and the TAR was 0.041 mmol/g (Fig. S7). The NO_3^- removal by the CESM was 54% that of the AC electrode when calculated based on the electrode mass. However, because the CESM was not activated, its surface area (13.0 m^2/g) was less than 1% of that of AC (2103.7 m^2/g). when normalizing NO_3^- electrosorption by surface area (mmol/m^2), NO_3^- removal by the CESM would reach 2.4 × 10^{-3} mmol/m^2, which was about two orders of magnitude higher than that of the AC electrode (Fig. 4c). These data suggest that the CESM has much higher affinity for NO_3^- than AC.

Detailed analyses found that NO_3^- adsorption by AC (0.057± 0.001 mmol/g) only accounted for 32.0% of the total anion removal (Fig. 4c). The selectivity of the AC electrode for NO_3^- over Cl^-, SO_4^{2-}, and $H_2PO_4^-$ were calculated to be 1.12 ± 0.04, 1.29 ± 0.21 and 2.19 ± 0.15, respectively (Fig. 4d). The values suggest that the AC electrode has little selectivity for NO_3^- over the competing Cl^-, SO_4^{2-}, and $H_2PO_4^-$. As a comparison, NO_3^- accounted for 75.6% of the total anion adsorption on CESM (Fig. 4c), more than two times of that for the AC electrode. The selectivity for NO_3^- over Cl^-, SO_4^{2-}, and $H_2PO_4^-$ of the CESM reached 7.79 ± 0.36, 10.38 ± 0.85, and 10.38 ± 0.62, respectively (Fig. 4d), much higher than the AC electrode.

The CESM produced a notably lower current than the AC electrode (Fig. S8&4e). However, the charge efficiency of the CESM (67.9 ± 4.2%) was much higher than AC (39.3 ± 1.8%) (Fig. 4e), indicating that charges provided to the CESM were more efficiently utilized for ion adsorption. This is attributed to the strong interactions between NO_3^- and adsorption sites on the CESM, and hence less interference from cations compared to the AC electrode. The high charge efficiency and NO_3^- selectivity of the CESM both decrease energy consumption for NO_3^- removal from the multi-solute solution. The energy consumption for NO_3^- removal from the multi-solute solution was 1147.7 kJ/mol-NO_3^- by the AC electrode, but only 248.8 kJ/mol-NO_3^- by the CESM, an almost 5-fold reduction.

3.4. Comparison with previous studies

Table 1 and Fig. 4f summarize the NO_3^-/Cl^- selectivity in electrosorption studies reported in the literature. These studies utilized different materials and different applied voltages to achieve selective electrosorption of NO_3^-. For example, NO_3^--selective ion exchange resin coatings on activated carbon electrodes were reported to reach NO_3^-/Cl^- selectivity of 2.3 at 1.0 V (Kim and Choi, 2012) and < 1.5 at 1.0–1.6 V (Gan et al., 2019). A quaternary amine functionalized carbon achieved NO_3^-/Cl^- selectivity of < 6.5 at voltage of 0.4 V (Oyarzun et al., 2018). An ultramicroporous carbon with sub nanometer pores realized NO_3^-/Cl^- selectivity of 6.1 at 0.6 V (Hawks et al., 2019) and 6.0 at 1.2 V(Mubita et al., 2019). Utilizing a commercial anion exchange membrane (Neosepta AMX) in CDI also realized NO_3^-/Cl^- selectivity of 4.37 at < 1.0 V (Kim et al., 2013). In our study, the CESM realized NO_3^-/Cl^- selectivity of 7.79 ± 0.36 at an applied voltage of 1.2 V. To the best of our knowledge, this NO_3^-/Cl^- selectivity was the highest to date among reported studies operating at 1.2 V (Fig. 4f, Table 1). It is well understood that the NO_3^-/Cl^- selectivity decreases with increasing applied voltage due to enhanced dehydration of Cl^- at higher voltages (Fig. 4f, Table 1). Therefore, it is expected that the NO_3^-/Cl^- selectivity of the CESM could be further improved if a lower voltage is applied. However, low operation voltage would lead to decreased electrosorption kinetics and overall electrosorption capacity, which would require longer adsorption time and more electrode materials to achieve the same removal. A good electrosorption material should possess high selectivity at high operation voltage (e.g., 1.2 V) to realize high selectivity, fast kinetics, as well as low electrode material usage for the removal of a target contaminant.

It is noted that Eq. (5) takes into consideration the influent concentrations of the target and competing ions. Therefore, selectivity calculated using Eq. (5) allows comparison between studies that used different Cl^- to NO_3^- concentration ratios if adsorption is linear with respect to influent concentration, which is usually the case at relatively low concentrations. The Cl^- to NO_3^- concentration ratios used in the previous studies shown in Table 1 ranged from 1:1 to 3:1. In this study, the Cl^-/NO_3^- concentration ratio (1:1) used was similar to many previous studies (Hassanvand et al., 2018; Hawks et al., 2019; Mubita et al., 2019; Tong and Elimelech, 2016; Tsai et al., 2021; Wang et al., 2020). This suggests that direct comparison of NO_3^-/Cl^- selectivity is reasonable. In real water and wastewater, however, the Cl^- to NO_3^- concentration ratio can be much higher than those used in these studies. Further research is needed to evaluate electrode materials' selectivity in more realistic solution conditions. In addition, the high NO_3^- concentration in the brine collected during the desorption step is favorable for N recovery as a nutrient. In the case degradation is required, a higher NO_3^- concentration will also enhance biological or (electro)chemical degradation rate.

3.5. Proposed mechanism of nitrate selective removal on CESM

Several factors influence electrosorption selectivity, including hydrated size, valence, and electronegativity of the ions (Eliad et al., 2001; Guyes et al., 2019; Hawks et al., 2019; Mubita et al., 2019; Sun et al., 2018; Suss, 2017), and pore size (Hawks et al., 2019) as well as the surface chemistry (Ma et al., 2019; Oyarzun et al., 2018; Palko et al., 2018) of the electrode. The NO_3^- and Cl^- ions have smaller hydrated ion radius than $H_2PO_4^-$ and SO_4^{2-}. Therefore, they have better access to the active sites and adsorption capacity. Despite that NO_3^- and Cl^- have similar hydrated radius (NO_3^-, 0.335 nm; Cl^-, 0.332 nm) and diffusion coefficients (NO_3^-, 1.91 × 10^{-9} m^2/s; Cl^-, 2.03 × 10^{-9} m^2/s) (Hassanvand et al., 2018), previous studies have reported that NO_3^- was preferentially removed by activated carbon electrodes, and the selectivity are attributed to its higher electronegativity (4.32) than Cl^- (3.16) (Sun et al., 2018) and weaker solvation, which allows NO_3^- to be easily dehydrated and adsorbed in small pores (Hawks et al., 2019). In our study, the AC possessed rich micropores with pore sizes < 2 nm (Fig. 2c); it realized slightly higher electrosorption of NO_3^- (0.057 ± 0.001 mmol/g) than Cl^- (0.051 ± 0.001 mmol/g) from the multi-solute solution, consistent with previous reports (Hawks et al., 2019; Sun et al., 2018). Although the CESM possessed much bigger pore sizes (>2.5 nm, Fig. 2b), it still achieved significantly higher NO_3^-/Cl^- selectivity. This result indicates that the pore size is not the main reason for the high NO_3^-/Cl^- selectivity found in CESM. We hypothesize that the high NO_3^- selectivity on CESM resulted from its different chemical composition and unique chemical interactions with NO_3^-.

As revealed by XPS, the AC electrode was mainly composed of C with no detectable N atoms (Fig. S9). The CESM, however, contained 13.3 wt % N and 6.2 wt% O (Fig. 5a). Many previous studies have reported that N-containing-amine functionalized activated carbon (Oyarzun et al., 2018; Palko et al., 2018) and ion exchange resins containing amine functional groups (Ebrahimi and Roberts, 2015; Gan et al., 2019; Kim and Choi, 2012) improve selective adsorption of NO_3^-. Therefore, it is hypothesized that the rich N species on the CESM are related to the superior NO_3^-/Cl^- selectivity. As shown in Fig. 5b, detailed XPS analysis of the N1s spectrum showed that the CESM contained four nitrogen species: pyridinic nitrogen (N-6, 398.44 eV), pyrrolic nitrogen (N-5, 399.7 eV), oxidized pyridinic nitrogen (N-X, 402.5 eV), and quaternary nitrogen (N-Q, 400.8 eV) (Fig. 5b) (Li et al., 2014; Xiao et al., 2013). The

Table 1
Nitrate selectivity in different electrosorption systems.

Electrode material (manufacturer)	Ion exchange membrane	Electrode size ($L \times W \times T$, in cm)	Solution (mM)	Operation mode (solution volume)	Flow rate (mL /min)	Ad/ desorption voltage (V)	Ad/ desorption time (min)	Selectivity	Ref.
Fruit-derived carbon HbioC	na	4 × 4 × 0.1	3.33, 3.33, 1.67 for Cl^-, NO_3^-, SO_4^{2-}	Batch (50 mL)	10	0.4/n	120/n	NO_3^-/Cl^- < 2* NO_3^-/SO_4^{2-} = 20.5*	(Wang et al., 2020)
						0.8/n		NO_3^-/Cl^- < 2* NO_3^-/SO_4^{2-} = 13.5	
						1.2/n		NO_3^-/Cl^- = 1.83 NO_3^-/SO_4^{2-} = 12.62	
Fruit-derived carbon bioC						0.4/n	120/n	NO_3^-/Cl^-< 6.5* NO_3^-/SO_4^{2-} = 15.7*	
						0.8/n		NO_3^-/Cl^- < 6.5* NO_3^-/SO_4^{2-} = 12.9	
						1.2/n		NO_3^-/Cl^- < 6.5* NO_3^-/SO_4^{2-} = 12.3	
Commercial AC (ACS20)	na	20 × 20 × 0.07	5, 5, for Cl^-, NO_3^-	Single pass	10	0.6/0	60/60	NO_3^-/Cl^- = 2.8	(Tsai et al., 2021)
						1.2/0		NO_3^-/Cl^- = 2.44	
						1.8/0		NO_3^-/Cl^- = 1.4	
	Neosepta AMX					0.6/0		NO_3^-/Cl^- = 1.5	
						1.2/0		NO_3^-/Cl^- = 1.28	
						1.8/0		NO_3^-/Cl^- = 1.08	
Commercial AC (Yi-Huan)	na	na	2, 2 for Cl^-, NO_3^-	Batch (50 mL)	n	1.2/n	50/n	NO_3^-/Cl^-= 1.44	(Tong and Elimelech, 2016)
Granular AC	na	5 × 4.5 × n	100 mg/L each for ReO_4^-, Cl^-, NO_3^-, SO_4^{2-}	Batch (4000 mL)	140	1.2/0	250/n	NO_3^-/Cl^- < 7*	(Sun et al., 2018)
Composite carbon	BHP55	*10 × 10 × n*	5, 2 for Cl^-, NO_3^-	Batch (300 mL)	50	1/0	15/10	NO_3^-/Cl^- < 4*	(Yeo and Choi, 2013)
Composite carbon	BHP55	*10 × 10 × n*	5, 2 for Cl^-, NO_3^-	Batch (300 mL)	50	1/0	15/10	NO_3^-/Cl^- = 3.39*	(Kim and Choi, 2012)
Composite carbon	Neosepta AMX							NO_3^-/Cl^-= 1.30*	
Composite carbon	Neosepta AMX	10 × 10 × n	5, 2 for Cl^-, NO_3^-	Batch (300 mL)	50	1/0	15/10	NO_3^-/Cl^- = 1.29*	(Kim et al., 2013)
Composite carbon	A520E	*8 × 8 × n*	2, 1 for Cl^-, NO_3^-	Batch (200 mL)	15	1.0/0	70/120	NO_3^-/Cl^- = 2.35*	(Gan et al., 2019)
						1.2/0		NO_3^-/Cl^-= 1.72*	
						1.4/0		NO_3^-/Cl^-= 1.43*	
						1.6/0		NO_3^-/Cl^- = 1.28*	
Commercial AC (Norit SA4)	na	10 × 20 × n	10, 10, 5 for Cl^-, NO_3^-, SO_4^{2-}	Single pass	20	1.5/0	10/10	NO_3^-/Cl^- = 1.45* NO_3^-/SO_4^{2-} = 1.33*	(Hassanvand et al., 2018)
	Neosepta AMX	10 × 20 × n				1.5/−1.5		NO_3^-/Cl^- = 1.24* NO_3^-/SO_4^{2-} = 1.36*	
Commercial AC (PACMM™)	na	S33.8 cm^2 × 0.025	※10, 10 for Cl^-, NO_3^-	Batch (160 mL)	30	1.2/0	10/n	NO_3^-/Cl^- = 6	(Mubita et al., 2019)
Functionalized AC	na	D3.5 cm × 0.025	2, 2 for Cl^-, NO_3^-	Single pass	0.43	0/0.4	120/120	NO_3^-/Cl^-= 6.5	(Oyarzun et al., 2018)
Ultramicroporous carbon aerogel	na	4 × 5.6 × n		Single pass	1	0.6/−0.6	30/30	NO_3^-/Cl^- = 6.1	(Hawks et al., 2019)

(*continued on next page*)

Table 1 (*continued*)

Electrode material (manufacturer)	Ion exchange membrane	Electrode size ($L \times W \times T$, in cm)	Solution (mM)	Operation mode (solution volume)	Flow rate (mL /min)	Ad/ desorption voltage (V)	Ad/ desorption time (min)	Selectivity	Ref.
			3.33, 3.33, 1.67 for Cl^-, NO_3^-, SO_4^{2-}			0.8/−0.8		NO_3^-/SO_4^{2-} = 17.8 NO_3^-/Cl^- = 4.5* NO_3^-/SO_4^{2-} = 14.5* 1.2/−1.2	
NO_3^-/Cl^- = 3.2 NO_3^-/SO_4^{2-} = 9.0									
Commercial AC (Beifang)	na	6 × 10 × 0.4	5, 5 for Cl^-, NO_3^-	Batch (700 mL)	20	1.2/n	200/n	NO_3^-/Cl^- = 1.6*	(Chen et al., 2015)
Composite carbon electrode	§Polymer coated	10 × 10, 50 pairs	2.26, 0.76, 0.46 for Cl^-, NO_3^-, SO_4^{2-}	Single pass	1.5	1.2/n	2/n	NO_3^-/Cl^- <6* NO_3^-/SO_4^{2-} <6*	(D.I. Kim et al., 2019)
CESM	CEM (ASTOM)	5 × 1 × 0.05	0.5, 0.5, 0.5, 0.5 for Cl^-, NO_3^-, SO_4^{2-}, $H_2PO_4^-$	Single pass	1	1.2/−1.2	30/30	NO_3^-/Cl^- = 7.75 NO_3^-/SO_4^{2-} = 10.33	This study
Commercial AC (CEP21K)								NO_3^-/Cl^- = 1.12 NO_3^-/SO_4^{2-} = 1.30	

NOTE: * Data calculated or estimated according to figures and profiles described in corresponding articles; n: data not available; All the electrolyte solutions are sodium solutions, except that ※ means the electrolyte is potassium salt solution; Γ: a constant current was applied until the cell potential reached 1.0 V; S: electrode area; D: diameter of the electrode. §:the polymer type were not found in the corresponding articles.

N-6 and N-5 are nitrogen atoms that are bonded with two carbon atoms and donate two s-electrons to the π-system of a 6- and 5-member ring, respectively; the N-X peak originates from oxidized pyridine nitrogen atoms that are bonded with two carbon atoms and one oxygen atom; the N-Q peak is related to nitrogen atoms that are connected with three carbon atoms via covalent bonds. It was reported that the N species could induce charge delocalization on the carbon matrix. Because the electronegativity of N (3.5) is higher than that of C (3.0) (Wang et al., 2011; Zheng et al., 2014), the charge on C atoms adjacent to N redistributes and reaches a substantially high positive charge density in order to counterbalance the strong electronic affinity of N. The redistributed charge can attract cations/anions and thus improve electrosorption for target species (Liu et al., 2020). It was also reported that the N-Q and N-X exhibited electron donor ability and could boost electron transfer kinetics through the carbon material (Cheng et al., 2019; Shen and Fan, 2013; Zhou et al., 2015), and the N-5 and N-6 may enhance electrosorption activity as they are located at the edge sites of the carbon matrix (Ji et al., 2018; Yang et al., 2019). In addition, the N species were also reported to improve the wettability of carbon, which was confirmed in this study by contact angle measurement (Fig. S10) and may improve the electrolyte invasion and ion adsorption.

To evaluate the effect of N species on electrosorption of anions on CESM, DFT calculation was performed to determine the molecular distance and binding energy between the nitrogen species on CESM and various anions including NO_3^-, Cl^- and SO_4^{2-}. As shown in Fig. 5c, the schematics illustrated the molecular structure and charge distribution of the nitrogen species on CESM and various anions. The calculated molecular distance between the N atoms on CESM and various anions showed that all the N species on CESM had the shortest distance to NO_3^- compared with Cl^- and SO_4^{2-} (Fig. 5d). The Gibbs free energy of the binding reactions between various N species on CESM and NO_3^- was negative and lower than that for Cl^- and SO_4^{2-} (Fig. 5e), implying stronger binding of NO_3^- than $Cl^-$and SO_4^{2-} on the CESM. Since the calculations were performed in hydrosolvent conditions, the high affinity of N species on CESM for NO_3^- may be attributed to the lower absolute hydration energy of NO_3^- (−300 kJ/mol) than Cl^- (−340 kJ/mol) and SO_4^{2-} (−1080 kJ/mol) (Hawks et al., 2019), which leads to a lower energy barrier for dehydration (Epsztein et al., 2019). Besides NO_3^-, it is also interesting to note that the various N species on CESM also have shorter distance and higher affinity for SO_4^{2-} than that of Cl^-, while Cl^- removal was higher than SO_4^{2-} in both the single solute solution (Fig. 3c) and the mixed solute solution (Fig. 4c). This result may be caused by the larger size of SO_4^{2-} (radius of 0.379 nm) than Cl^- (0.332 nm), which leads to less accessibility of SO_4^{2-} to the CESM pores. Notably, the N-6 and N-X show smaller closest-distance to NO_3^- than N-Q and N-5 (Fig. 5d), and their binding energy is also higher than N-Q (Fig. 5e), suggesting that they may have greater effect on NO_3^- electrosorption. Further experiments are needed to test this hypothesis using electrode materials doped with single nitrogen species.

The carbonization temperature was found to have an important impact on the performance of the CESM electrode. As shown in Fig. S11, the CESM carbonized at 400 °C exhibited negligible salt electrosorption, presumably due to incomplete carbonization and hence low conductance. The CESM carbonized at 800 °C, on the other hand, showed higher adsorption capacity for both NO_3^- (0.038 mmol/g) and Cl^- (0.009 mmol/g) than the CESM carbonized at 600 °C (Table S1). The higher adsorption capacity may be attributed to the higher specific surface area and electric conductivity resulting from the higher carbonization temperature. Nevertheless, the CESM carbonized at 800 °C obtained a NO_3^-/Cl^- selectivity (4.16) much lower than the CESM carbonized at 600 °C. These results indicate that carbonization at high temperatures (e.g., 800 °C) may damage the nitrogen functional groups that are responsible for NO_3^-selectivity.

4. Conclusion

In this study, an ultrathin porous electrode derived from the eggshell bio-wastes was fabricated and for the first time utilized in electrosorption for removal of anionic species. The prepared carbonized eggshell membrane possessed an interconnected porous network with a uniform micrometer thickness and a hierarchical pore size ranging from several tens of microns to a few nanometers. Although CESM has low specific surface area, it has high electric capacitance and realized surface-area normalized ion adsorption capacity two orders of magnitude higher than activated carbon. More importantly, the CESM exhibited to date the highest selectivity for NO_3^- against common

competing anions including Cl^-, SO_4^{2-}, and $H_2PO_4^-$. DFT calculations revealed the critical role of the abundant nitrogen-containing functional groups on CESM in selective adsorption of NO_3^-, a great advantage of carbon materials derived from protein rich biowaste. These findings are particularly encouraging because they not only suggest that nitrogen-rich biomaterials are promising precursors for NO_3^- selective electrodes, but also provide an important direction for chemical modification of other material systems where selective NO_3^- adsorption is needed. From a practical application aspect, the as synthesized CESM may not be an economical electrode material yet due to its low specific surface area. Further activation of the CESM or other nitrogen-rich biomaterials can be performed to introduce micropores and increase specific surface area. Alternatively, existing carbon electrode materials with high specific surface area can be functionalized to introduce nitrogen-containing function groups, e.g., by doping with N species to further enhance the NO_3^- selectivity. In addition, the stability of the CESM also needs to be investigated during long-term operation. These nitrogen rich electrode materials have the potential to remove and recover NO_3^- from water and wastewater through highly selective electrosorption processes.

Declaration of Competing Interest

The authors declare that they have no known competing financial interests or personal relationships that could have appeared to influence the work reported in this paper.

Acknowledgement

This work was supported by the NSF Nanosystems Engineering Research Center for Nanotechnology-Enabled Water Treatment (EEC-1449500) and National Natural Science Foundation of China (No. 51978369).

Supplementary materials

Supplementary material associated with this article can be found, in the online version, at doi:10.1016/j.watres.2022.118351.

References

Ahualli, S., Orozco-Barrera, S., Fernández, M.d.M., Delgado, Á.V., Iglesias, G.R, 2019. Assembly of soft electrodes and ion exchange membranes for capacitive deionization. Polymers 11 (10), 1556.
Almasri, M.N., 2007. Nitrate contamination of groundwater: a conceptual management framework. Environ. Impact Assess. Rev. 27 (3), 220–242.
Arami, M., Yousefi Limaee, N., Mahmoodi, N.M, 2006. Investigation on the adsorption capability of egg shell membrane towards model textile dyes. Chemosphere 65 (11), 1999–2008.
Chen, Z., Zhang, H., Wu, C., Wang, Y., Li, W., 2015. A study of electrosorption selectivity of anions by activated carbon electrodes in capacitive deionization. Desalination 369, 46–50.
Cheng, J., Xu, Q.Q., Wang, X., Li, Z.Q., Wu, F.Z., Shao, J.J., Xie, H.B, 2019. Ultrahigh-surface-area nitrogen-doped hierarchically porous carbon materials derived from chitosan and betaine hydrochloride sustainable precursors for high-performance supercapacitors. Sustain Energy Fuels 3 (5), 1215–1224.
Deng, Y.F., Xie, Y., Zou, K.X., Ji, X.L, 2016. Review on recent advances in nitrogen-doped carbons: preparations and applications in supercapacitors. J Mater Chem A 4 (4), 1144–1173.
Ebrahimi, S., Roberts, D.J, 2015. Bioregeneration of single use nitrate selective ion-exchange resin enclosed in a membrane: kinetics of desorption. Sep. Purif. Technol. 146, 268–275.
Eliad, L., Salitra, G., Soffer, A., Aurbach, D., 2001. Ion sieving effects in the electrical double layer of porous carbon electrodes: estimating effective ion size in electrolytic solutions. J. Phys. Chem. B 105 (29), 6880–6887.
Epsztein, R., Shaulsky, E., Qin, M., Elimelech, M., 2019. Activation behavior for ion permeation in ion-exchange membranes: role of ion dehydration in selective transport. J. Membr. Sci. 580, 316–326.
Gan, L., Wu, Y.F., Song, H.O., Zhang, S.P., Lu, C., Yang, S., Wang, Z., Jiang, B.C., Wang, C.M., Li, A.M, 2019. Selective removal of nitrate ion using a novel activated carbon composite carbon electrode in capacitive deionization. Sep. Purif. Technol. 212, 728–736.
Geng, J., Wu, H., Al-Enizi, A.M., Elzatahry, A.A., Zheng, G., 2015. Freestanding eggshell membrane-based electrodes for high-performance supercapacitors and oxygen evolution reaction. Nanoscale 7 (34), 14378–14384.
Grimme, S., 2011. Density functional theory with London dispersion corrections. WIREs Comput. Mol. Sci. 1 (2), 211–228.
Guyes, E.N., Malka, T., Suss, M.E, 2019. Enhancing the ion-size-based selectivity of capacitive deionization electrodes. Environ. Sci. Technol. 53 (14), 8447–8454.
Han, X., Wang, W., Zuo, K., Chen, L., Yuan, L., Liang, J., Li, Q., Ajayan, P.M., Zhao, Y., Lou, J., 2019. Bio-derived ultrathin membrane for solar driven water purification. Nano Energy 60, 567–575.
Hassanvand, A., Chen, G.Q., Webley, P.A., Kentish, S.E, 2018. A comparison of multicomponent electrosorption in capacitive deionization and membrane capacitive deionization. Water Res. 131, 100–109.
Hawks, S.A., Ceron, M.R., Oyarzun, D.I., Pham, T.A., Zhan, C., Loeb, C.K., Mew, D., Deinhart, A., Wood, B.C., Santiago, J.G., Stadermann, M., Campbell, P.G, 2019. Using ultramicroporous carbon for the selective removal of nitrate with capacitive deionization. Environ. Sci. Technol. 53 (18), 10863–10870.
Humphrey, W., Dalke, A., Schulten, K., 1996. VMD: visual molecular dynamics. J. Mol. Graph. 14 (1), 33–38.
Ismagilov, Z.R., Shalagina, A.E., Podyacheva, O.Y., Ischenko, A.V., Kibis, L.S., Boronin, A.I., Chesalov, Y.A., Kochubey, D.I., Romanenko, A.I., Anikeeva, O.B., Buryakov, T.I., Tkachev, E.N, 2009. Structure and electrical conductivity of nitrogen-doped carbon nanofibers. Carbon 47 (8), 1922–1929.
Jain, A., Kim, J., Owoseni, O.M., Weathers, C., Cana, D., Zuo, K.C., Walker, W.S., Li, Q.L., Verduzco, R., 2018. Aqueous-processed, high-capacity electrodes for membrane capacitive deionization. Environ. Sci. Technol. 52 (10), 5859–5867.
Ji, Q.H., Hu, C.Z., Liu, H.J., Qu, J.H, 2018. Development of nitrogen-doped carbon for selective metal ion capture. Chem. Eng. J. 350, 608–615.
Johnson, E., Becke, A., 2005. A post-Hartree–Fock model of intermolecular interactions. J. Chem. Phys. 123, 24101.
Kälble, T., Tricker, A.R., Möhring, K., Berger, M.R., Geiss, H., Staehler, G., 1990. The role of nitrate, nitrite and N-nitrosamines in carcinogenesis of colon tumours following ureterosigmoidostomy. Urol. Res. 18 (2), 123–129.
Kim, D.I., Dorji, P., Gwak, G., Phuntsho, S., Hong, S., Shon, H., 2019a. Reuse of municipal wastewater via membrane capacitive deionization using ion-selective polymer-coated carbon electrodes in pilot-scale. Chem. Eng. J. 372, 241–250.
Kim, Y.J., Choi, J.H, 2012. Selective removal of nitrate ion using a novel composite carbon electrode in capacitive deionization. Water Res. 46 (18), 6033–6039.
Kim, Y.J., Kim, J.H., Choi, J.H, 2013. Selective removal of nitrate ions by controlling the applied current in membrane capacitive deionization (MCDI). J. Membr. Sci. 429, 52–57.
Kong, J., Yu, S., 2007. Fourier transform infrared spectroscopic analysis of protein secondary structures. Acta Biochim. Biophys. Sin. 39 (8), 549–559.
Li, Q., Huang, B., Chen, X., Shi, Y., 2015. Cost-effective bioregeneration of nitrate-laden ion exchange brine through deliberate bicarbonate incorporation. Water Res. 75, 33–42.
Li, X., Liang, J., Hou, Z., Zhu, Y., Qian, Y., 2014. Recycling chicken eggshell membranes for high-capacity sodium battery anodes. RSC Adv. 4 (92), 50950–50954.
Li, Y., Liu, Y.X., Shen, J.M., Qi, J.W., Li, J.S., Sun, X.Y., Shen, J.Y., Han, W.Q., Wang, L.J, 2018. Design of nitrogen-doped cluster-like porous carbons with hierarchical hollow nanoarchitecture and their enhanced performance in capacitive deionization. Desalination 430, 45–55.
Li, Z., Zhang, L., Amirkhiz, B.S., Tan, X., Xu, Z., Wang, H., Olsen, B.C., Holt, C.M.B., Mitlin, D., 2012. Carbonized chicken eggshell membranes with 3D architectures as high-performance electrode materials for supercapacitors. Adv. Energy Mater. 2 (4), 431–437.
Liang, M., Su, R., Huang, R., Qi, W., Yu, Y., Wang, L., He, Z., 2014. Facile in situ synthesis of silver nanoparticles on procyanidin-grafted eggshell membrane and their catalytic properties. ACS Appl. Mater. Interfaces 6 (7), 4638–4649.
Liu, B., Huang, Y., 2011. Polyethyleneimine modified eggshell membrane as a novel biosorbent for adsorption and detoxification of Cr(VI) from water. J. Mater. Chem. 21 (43).
Liu, T., Serrano, J., Elliott, J., Yang, X., Liu, G., 2020. Exceptional capacitive deionization rate and capacity by block copolymer-based porous carbon fibers. Sci. Adv. 6 (16), 0906.
Lytle, J.C., Wallace, J.M., Sassin, M.B., Barrow, A.J., Long, J.W., Dysart, J.L., Renninger, C.H., Saunders, M.P., Brandell, N.L., Rolison, D.R, 2011. The right kind of interior for multifunctional electrode architectures: carbon nanofoam papers with aperiodic submicrometre pore networks interconnected in 3D. Energy Environ. Sci. 4 (5).
Ma, D.Y., Cai, Y.M., Wang, Y., Xu, S.C., Wang, J.X., Khan, M.U, 2019. Grafting the charged functional groups on carbon nanotubes for improving the efficiency and stability of capacitive deionization process. ACS Appl. Mater. Interfaces 11 (19), 17617–17628.
Marcus, Y., 1991. Thermodynamics of solvation of ions. Part 5.—Gibbs free energy of hydration at 298.15K. J. Chem. Soc., Faraday Trans. 87 (18), 2995–2999.
Marenich, A.V., Cramer, C.J., Truhlar, D.G, 2009. Universal solvation model based on solute electron density and on a continuum model of the solvent defined by the bulk dielectric constant and atomic surface tensions. J. Phys. Chem. B 113 (18), 6378–6396.
Meng, X.Y., Vaccari, D.A., Zhang, J.F., Fiume, A., Meng, X.G, 2014. Bioregeneration of spent anion exchange resin for treatment of nitrate in water. Environ. Sci. Technol. 48 (3), 1541–1548.
Mubita, T.M., Dykstra, J.E., Biesheuvel, P.M., van der Wal, A., Porada, S., 2019. Selective adsorption of nitrate over chloride in microporous carbons. Water Res. 164.

Mulliken, R.S., 1955. Electronic population analysis on lcao-mo molecular wave functions .4. Bonding and antibonding in lcao and valence-bond theories. J. Chem. Phys. 23 (12), 2343–2346.
Oyarzun, D.I., Hemmatifar, A., Palko, J.W., Stadermann, M., Santiago, J.G, 2018. Ion selectivity in capacitive deionization with functionalized electrode: theory and experimental validation. Water Res. X 1, 100008.
Palko, J.W., Oyarzun, D.I., Ha, B., Stadermann, M., Santiago, J.G, 2018. Nitrate removal from water using electrostatic regeneration of functionalized adsorbent. Chem. Eng. J. 334, 1289–1296.
Pastushok, O., Zhao, F., Ramasamy, D.L., Sillanpää, M., 2019. Nitrate removal and recovery by capacitive deionization (CDI). Chem. Eng. J. 375, 121943.
Porada, S., Zhao, R., van der Wal, A., Presser, V., Biesheuvel, P.M, 2013. Review on the science and technology of water desalination by capacitive deionization. Prog. Mater. Sci. 58 (8), 1388–1442.
Rath, M.K., Choi, B.-.H., Ji, M.-.J., Lee, K.-.T, 2014. Eggshell-membrane-templated synthesis of hierarchically-ordered NiO–Ce0.8Gd0.2O1.9 composite powders and their electrochemical performances as SOFC anodes. Ceram. Int. 40 (2), 3295–3304.
Romano, N., Zeng, C., 2007. Effects of potassium on nitrate mediated alterations of osmoregulation in marine crabs. Aquat. Toxicol. 85 (3), 202–208.
Ruiz-Beviá, F., Fernández-Torres, M.J., 2019. Effective catalytic removal of nitrates from drinking water: an unresolved problem? J. Clean. Prod. 217, 398–408.
Sha Wang, M.W., Yuming, Huang, 2013. Biosorption of multifold toxic heavy metal ions from aqueous water onto food residue eggshell membrane functionalized with ammonium thioglycolate. Agric. Food Chem. 61, 4988–4996.
Shen, W.Z., Fan, W.B., 2013. Nitrogen-containing porous carbons: synthesis and application. J. Mater. Chem. A 1 (4), 999–1013.
Sun, Z.M., Chai, L.Y., Liu, M.S., Shu, Y.D., Li, Q.Z., Wang, Y.Y., Qiu, D.F, 2018. Effect of the electronegativity on the electrosorption selectivity of anions during capacitive deionization. Chemosphere 195, 282–290.
Sunho Park, K.S.C., 2016. Eggshell membrane: review and impact on engineering. Biosystem Eng. 151, 446–463.
Suss, M.E., 2017. Size-based ion selectivity of micropore electric double layers in capacitive deionization electrodes. J. Electrochem. Soc. 164 (9), E270–E275.
Suss, M.E., Porada, S., Sun, X., Biesheuvel, P.M., Yoon, J., Presser, V., 2015. Water desalination via capacitive deionization: what is it and what can we expect from it? Energy Environ. Sci. 8 (8), 2296–2319.
Tong, T.Z., Elimelech, M., 2016. The global rise of zero liquid discharge for wastewater management: drivers, technologies, and future directions. Environ. Sci. Technol. 50 (13), 6846–6855.
Tsai, S.-.W., Hackl, L., Kumar, A., Hou, C.-.H, 2021. Exploring the electrosorption selectivity of nitrate over chloride in capacitive deionization (CDI) and membrane capacitive deionization (MCDI). Desalination 497.
Tsai, W.T., Yang, J.M., Lai, C.W., Cheng, Y.H., Lin, C.C., Yeh, C.W, 2006. Characterization and adsorption properties of eggshells and eggshell membrane. Bioresour Technol. 97 (3), 488–493.
Uzun, H.I., Debik, E., 2019. Economical approach to nitrate removal via membrane capacitive deionization. Sep. Purif. Technol. 209, 776–781.
Wang, H., Deng, H., He, Y., Huang, L., Wei, D., Hao, T., Wang, S., Jin, L., Zhang, L., 2020. Facile and sustainable synthesis of slit-like microporous N-doped carbon with unexpected electrosorption performance. Chem. Eng. J. 396, 125249.
Wang, H.B., Zhang, C.J., Liu, Z.H., Wang, L., Han, P.X., Xu, H.X., Zhang, K.J., Dong, S.M., Yao, J.H., Cui, G.L, 2011. Nitrogen-doped graphene nanosheets with excellent lithium storage properties. J. Mater. Chem. 21 (14), 5430–5434.
Wang, T., Zhang, S., Yan, X., Lyu, M., Wang, L., Bell, J., Wang, H., 2017. 2-methylimidazole-derived Ni-Co Layered double hydroxide nanosheets as high rate capability and high energy density storage material in hybrid supercapacitors. ACS Appl. Mater. Interfaces 9 (18), 15510–15524.
Xiao, N., Lau, D., Shi, W., Zhu, J., Dong, X., Hng, H.H., Yan, Q., 2013. A simple process to prepare nitrogen-modified few-layer graphene for a supercapacitor electrode. Carbon N Y 57, 184–190.
Xu, D., Tong, Y., Yan, T., Shi, L., Zhang, D., 2017. N,P-codoped meso-/microporous carbon derived from biomass materials via a dual-activation strategy as high-performance electrodes for deionization capacitors. ACS Sustain. Chem. Eng. 5 (7), 5810–5819.
Xu, X.T., Allah, A.E., Wang, C., Tan, H.B., Farghali, A.A., Khedr, M.H., Malgras, V., Yang, T., Yamauchi, Y., 2019. Capacitive deionization using nitrogen-doped mesostructured carbons for highly efficient brackish water desalination. Chem. Eng. J. 362, 887–896.
Yang, D., Song, Y., Ye, Y.J., Zhang, M.Y., Sun, X.Q., Liu, X.X, 2019. Boosting the pseudocapacitance of nitrogen-rich carbon nanorod arrays for electrochemical capacitors. J Mater Chem A 7 (19), 12086–12094.
Yeo, J.-.H., Choi, J.-.H, 2013. Enhancement of nitrate removal from a solution of mixed nitrate, chloride and sulfate ions using a nitrate-selective carbon electrode. Desalination 320, 10–16.
Zhang, L., Li, J., Zhu, X., Ye, D.-d., Liao, Q., 2015. Effect of proton transfer on the performance of unbuffered tubular microbial fuel cells in continuous flow mode. Int. J. Hydrogen Energy 40 (10), 3953–3960.
Zheng, F.C., Yang, Y., Chen, Q.W, 2014. High lithium anodic performance of highly nitrogen-doped porous carbon prepared from a metal-organic framework. Nat. Commun. 5, 5261.
Zhou, L., Cao, H., Zhu, S.Q., Hou, L.R., Yuan, C.Z, 2015. Hierarchical micro-/mesoporous N- and O-enriched carbon derived from disposable cashmere: a competitive cost-effective material for high-performance electrochemical capacitors. Green Chem. 17 (4), 2373–2382.
Zuo, K., Huang, X., Liu, X., Gil Garcia, E.M., Kim, J., Jain, A., Chen, L., Liang, P., Zepeda, A., Verduzco, R., Lou, J., Li, Q, 2020. A hybrid metal–organic framework–reduced graphene oxide nanomaterial for selective removal of chromate from water in an electrochemical process. Environ. Sci. Technol. 54 (20), 13322–13332.
Zuo, K., Kim, J., Jain, A., Wang, T., Verduzco, R., Long, M., Li, Q., 2018. Novel composite electrodes for selective removal of sulfate by the capacitive deionization process. Environ. Sci. Technol. 52 (16), 9486–9494.